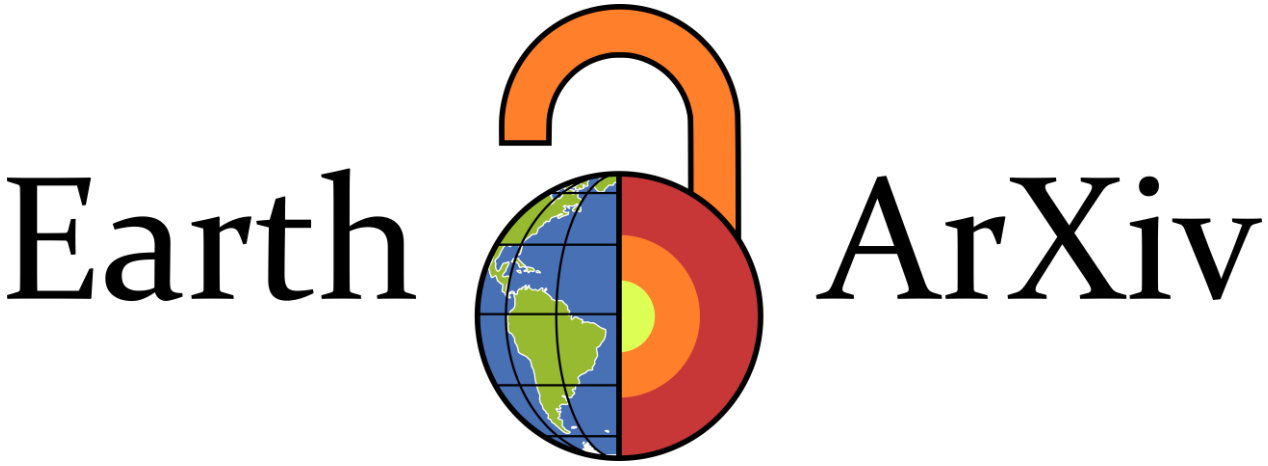

Tilting of Subsurface Floats due to Surface Waves

Eric A. D'Asaro[ab] and Andrey Y. Shcherbina[a]

[a] *Applied Physics Laboratory, University of Washington, Seattle, WA, USA*

[b] *School of Oceanography, University of Washington*

Corresponding author: Eric A D'Asaro, dasaro@apl.washington.edu

ABSTRACT: Subsurface and nearly neutrally-buoyant floats can be stable, well-behaved platforms for measuring ocean dynamics in the near-surface wave zone. Here, we measure and model the wave-induced tilt of one such platform. We use data from Lagrangian floats built at the Applied Physics Laboratory (APL/UW) and carrying a Nortek Signature1000 Acoustic Doppler Current Profiler with an AHRS (Attitude and Heading Reference System). We analyze carefully chosen data segments where the wave-induced tilts are measurable yet small and the float does not rotate significantly. We adopt a two-dimensional, depth-downwave coordinate system and assume small tilts and linear surface wave dynamics. By combining the constraints due to geometry, a wave-following float, and wave dynamics, we link measurements of both linear and angular acceleration to measure the tilts to an accuracy of a few tenths of a degree and simultaneously show that the data is consistent with the analysis assumptions. This analysis is further vetted by swinging the AHRS on pendulums in the laboratory. The same tests disturbingly indicate that the AHRS attitude readings can have large errors for tilts larger than a few degrees. The wave-induced tilt of the floats is predicted to an accuracy of about 10% from the wave properties by a 3-parameter linear semi-empirical model calibrated with field data. The waves force tilt through their horizontal acceleration and through their strain exerting torques on the float. These floats are a somewhat underdamped oscillator (Quality Factor=3, resonance at 3 second period) and will exhibit a decaying oscillation of a few cycles when perturbed.

SIGNIFICANCE STATEMENT: Accurate measurements of the ocean near the surface often require a detailed understanding of the motion of the platform caused by waves. Here, we model the vertical and horizontal motion and tilts of a subsurface oceanographic float near the surface and tune the model parameters using field data aided by laboratory measurements.

1. Introduction

The upper few meters of the ocean are an important region for horizontal transport, air-sea exchange, surface wave dynamics, and the interpretation of remote sensing data. Although near-surface currents are routinely measured by the global array of surface drifters (Centurioni et al. 2019), simulated by operational and research models (Menemenlis et al. 2008) and discussed in thousands of papers, detailed current measurements in the top few meters remain limited. A clear understanding of the structure of velocity in this region remains an area of active research, e.g. Laxague et al. (2018), Pizzo et al. (2019). The prospect of global surface current measurements by satellite (Ardhuin et al. 2019; Wineteer et al. 2020; Torres et al. 2023) makes the development of complementary measurement techniques particularly timely. For in situ measurements, surface waves usually produce motion and tilting of the measurement platform and possible contamination of the measurement by platform wakes. These factors are particularly detrimental to near-surface current measurements because the wave velocities are typically much larger than the low-frequency velocities and can often not be removed by averaging alone due to nonlinearities intrinsic in the measurement system or induced by the platform motion. Shcherbina and D'Asaro (2025), following earlier work (Pollard 1973; Amador et al. 2017; Thomson et al. 2019), analyze this problem in detail for a variety of platforms.

Neutrally buoyant (Gould 2005) and profiling (Wenstrand 1979; Luyten and Swallow 1976) floats have been used since the 1960s to measure ocean currents and current profiles. Floats are particularly attractive platforms for near-surface measurements: Since they move with the water, they can safely operate in even the most severe weather (D'Asaro and McNeil 2007) and can easily profile very near the surface. Operated as water-following Lagrangian instruments (D'Asaro 2003), they naturally measure horizontal, and, importantly, vertical velocity from their own motion. Additionally, ambient currents can be measured from the voltage across the float induced by the water's motion through the geomagnetic field (Sanford et al. 1978) or using float-

mounted Acoustic Doppler Current Profilers (ADCPs) (Shcherbina et al. 2018; Kumar et al. 2019; D'Asaro et al. 2018; Shcherbina et al. 2019). Below the influence of surface waves, the floats are very stable with typical RMS tilts of a fraction of a degree, which introduces only small errors into ADCP velocity measurements. However, surface waves induce oscillatory motion and tilt as a float approaches the surface. Shcherbina and D'Asaro (2025) show that these lead to velocity measurement errors comparable to the Stokes drift of the surface wave.

Here, we measure and model the wave-induced tilting of APL Lagrangian floats (MLFs). Lagrangian floats are neutrally buoyant and thus accurately follow the motion of water parcels larger than the float since both the water and the float are accelerated by the same wave pressure gradients as justified in detail by D'Asaro (2003, 2015). The float spatially averages waves smaller than itself (Lien et al. 1998) and is therefore not Lagrangian for these higher frequency waves. D'Asaro (2015) describes corrections for this effect, but these are not implemented here. Our analysis therefore applies only for a limited range of frequencies bounded by the lower end of the wave band, here 0.05 Hz, and the frequency above which the floats are not Lagrangian, here 0.4 Hz. Section a reviews the relevant properties of surface waves. Section 3 describes the floats and measurements.

Section 4 discusses various ways of accurately measuring float tilt in presence of lateral accelerations. We derive the kinematic relationships between the tilt of the float θ, the measurements of acceleration components ($\widehat{A}_x$, $\widehat{A}_z$) and the rotation rate ($\widehat{\Omega}_y$) on the float, assuming that the tilt is due to surface waves. The analysis results in two independent measurements of the tilt and thus consistency tests on the validity of the analysis assumptions. Section 5 applies this analysis to the Lagrangian float data and to supporting laboratory measurements (see Supplementary Material, SM). The two measurements are consistent, which justifies the analysis approach. The response of the float to the surface wave forcing is computed as a function of frequency.

Section 6 formulates and evaluates a model of the float tilt. The approach is semi-empirical, using theory to identify the relevant physics but not to derive the exact equations. Guided by these dynamics, a governing equation is proposed with physically interpretable parameters. These are estimated by fitting the model form to the data. The model fits the float frequency response with an error of about 10% rms, thus justifying this approach. The final product is the model form and parameters for two different data sets.

The analyzes assume that all angles are small and the surface waves are linear, both of which will be satisfied if the wave slope is small. We assume that the accelerations are much less than g, so all angles are small and proportional to the amplitude. Products of angles are second order in wave amplitude and will be ignored. The waves are assumed to vary only in the $x-z$ plane. The analysis follows the mathematical convention (Fig. 1C) using the right-hand rule to define angles with $\hat{z}$ pointing upward. Thus, positive angles in the $x-z$ plane appear clockwise when viewed looking in the $\hat{y}$ direction as in Fig. 1C and positive angles in the $x-y$ plane are anti-clockwise when viewed from above. The acceleration of gravity has a magnitude g and a vector $\vec{g} = -g\hat{z}$, so that a free-falling particle accelerates downward with $\vec{a} = \vec{g}$ and $a_z = -g$. The numerous symbols used in the analysis are listed and explained in Table 1.

2. Wave Properties

a. Basic Equations

We follow Phillips (1977) (P77) section 3.2 and specify a two-dimensional deep water surface wave by its vertical surface displacements (P77 3.2.1)

$$\zeta = \mathfrak{a}\cos(kx - \omega t) \tag{1}$$

where $\mathfrak{a}$ is the wave amplitude, k is the wavenumber, $\omega^2 = gk$ and g is the magnitude of gravitational acceleration. Using P77 (3.2.4, 2.4.19) the upward and eastward components of velocity are

$$w = \mathfrak{a}\omega e^{kz}\sin(kx - \omega t) \tag{2}$$

$$u = \mathfrak{a}\omega e^{kz}\cos(kx - \omega t) \tag{3}$$

and accelerations in the $\hat{z}$ and $\hat{x}$ directions are

$$a_z = \frac{\partial w}{\partial t} = -\mathfrak{a}\omega^2 e^{kz}\cos(kx - \omega t) \tag{4}$$

$$a_x = \frac{\partial u}{\partial t} = \mathfrak{a}\omega^2 e^{kz}\sin(kx - \omega t). \tag{5}$$

In first order in the small parameter $\mathfrak{a}k$, the vertical and horizontal displacements of particles from the initial positions z_0 and x_0 are

$$\xi = \int_0^t w(\vec{x}_0, t)dt = \mathfrak{a}e^{kz}\cos(kx - \omega t) \tag{6}$$

$$\chi = \int_0^t u(\vec{x}_0, t)dt = -\mathfrak{a}e^{kz}\sin(kx - \omega t) \tag{7}$$

respectively. The resulting wave surface, velocity vectors, orbital Lagrangian trajectories, and the distortion of fluid lines are shown in Fig. 1AB.

b. Wave Tilt and Strain Kinematics

In still water, a subsurface float with a stable righting moment will orient itself along the direction of the gravity vector $\vec{g}$, usually with its longest axis aligned vertically. More generally, its orientation will seek the direction of local "effective gravity" $\vec{g_e}$ defined as the sum of the gravity $\vec{g}$ and the negative of acceleration vectors

$$\vec{g_e} = \vec{g} - a_x\vec{x} - a_z\vec{z} \tag{8}$$

where g is the magnitude of $\vec{g}$ and $\vec{x}$ and $\vec{z}$ are the unit vectors in the x and z directions, respectively (Fig. 1c). In this notation, a free-falling particle accelerates at $\vec{g}$, $a_z = -g, a_x = 0$, and $g_e = 0$.

The $\vec{g}_e$ vector is shown as the red lines in Fig. 1AB. The angle of $\vec{g_e}$ from $-\vec{z}$ (down) is

$$\theta_G \approx \frac{a_x}{g} = \mathfrak{a}ke^{kz}\sin(kx - \omega t). \tag{9}$$

In the presence of waves, θ_G on a water-following float continually changes with time, causing a float with a righting moment to tilt, as will be investigated in great detail below.

The green lines in Fig. 1AB show the tilts of a surface of constant pressure. They will be called 'P-lines'. The P-lines tilt in the same way as the surface, since they are both surfaces of constant pressure.

$$\theta_P = \frac{\pi}{2} - \frac{\partial\xi}{\partial x} = \frac{\pi}{2} + \mathfrak{a}ke^{kz}\sin(kx - \omega t) = \frac{\pi}{2} + \theta_G. \tag{10}$$

θ_P is perpendicular to θ_G.

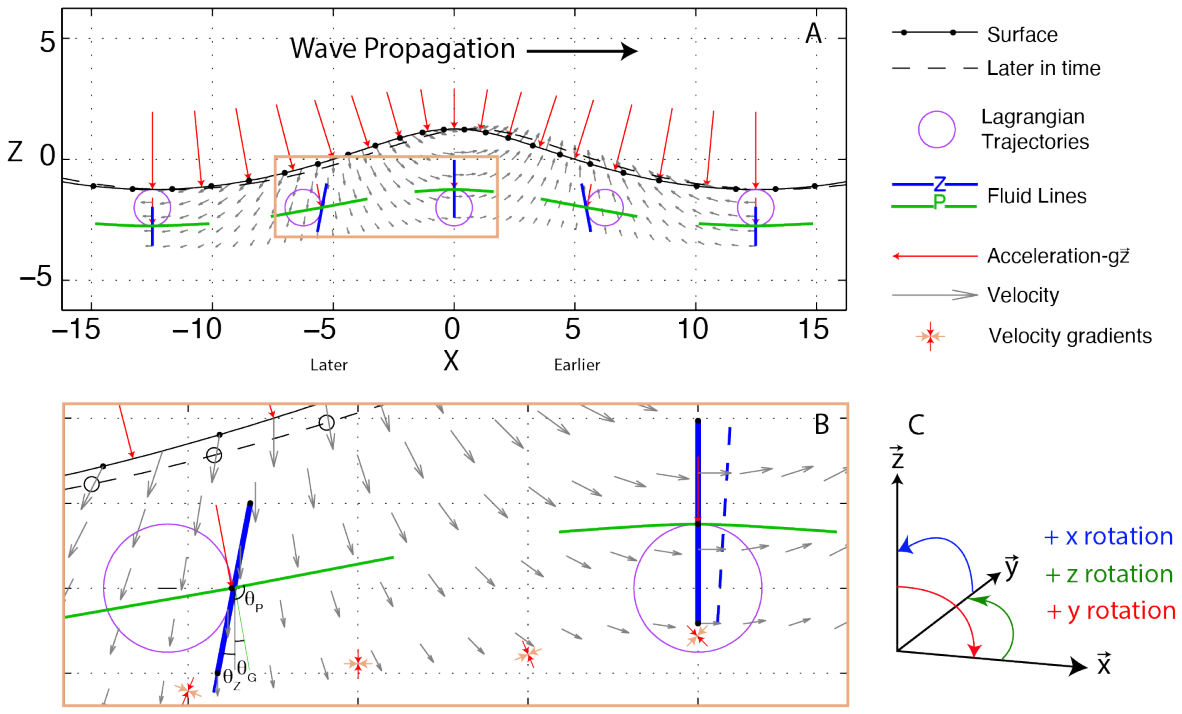

FIG. 1. A) and B) Kinematics of a monochromatic linear surface wave. B) is zoom of orange box in A). The Wave propagates in the +x direction, to the right. Wave phase varies horizontally with a wavelength of 25. The black line with dots marks the surface; the dashed black line shows the surface at a somewhat later time. Red lines mark the direction of effective gravity (8), i.e. gravitational acceleration + fluid acceleration. These are perpendicular to pressure surfaces; at the water surface they are perpendicular to the surface. Circles (purple) show representative Lagrangian trajectories of fluid parcels. Green lines at 5 different locations show the positions of fluid lines of constant pressure. These lines are nearly horizontal and will be called the 'P-lines'. Lagrangian particles follow surfaces of constant pressure to at least second order (D'Asaro 2015) so the P-lines also mark the motion of a nearly horizontal line of particles. Blue lines mark lines of fluid that would be vertical at the top of the wave; they will be 'Z-lines'. The P-lines and the surface remain perpendicular to the direction of the effective gravity, while the Z-lines tilt in the opposite direction with the same magnitude. The changing angles between the P- and Z-lines illustrates the straining of the fluid by the wave. The velocity gradients responsible are shown by the red and orange arrows. C) Coordinate definition. Rotation angles obey the right-hand rule so that a positive tilt angle θ is clockwise when viewed looking toward $+y$ as in this figure.

The blue lines in Fig. 1AB show the tilt of a fluid line that would be vertical in the absence of waves. They will be called 'Z-lines'. From (8)

$$\theta_Z = \frac{\partial \chi}{\partial z} = -\mathfrak{a} k e^{kz} \sin(kx - \omega t) = -\theta_G \tag{11}$$

The Z- and P-lines tilt in opposite directions with a magnitude of θ_G so that there is no net rotation of a fluid parcel, only straining, as required for potential flow. The tilting of Z-lines corresponds to the 'Inertial' case described by Longuet-Higgins (1986), his figure 21; the tilting of P-lines corresponds to his 'Hydrostatic' case.

3. Ocean Measurements

FIG. 2. Lagrangian float with a Nortek Signature ADCP and two CTDs. Inset shows a slightly different model of the float with the drogue open. The float displaces about 53 L and is 1.4 m long between the two CTDs; the main tube is 254 mm in diameter.

a. Setting

Measurements were made as part of two Departmental Research Initiatives of the Office of Naval Research: Waves, Langmuir Cells, and the Upper Ocean Boundary Layer (LCDRI) and Coherent

Lagrangian Pathways from the Surface Ocean to Interior (CALYPSO). LCDRI measurements were made during March and April 2017 between Catalina and San Nicolas Island off the coast of southern California (Ma et al. 2020). During the 17 days of operation, the wind varied from nearly calm to 18 m / s, producing a wide range of wind and wave conditions, resulting in four major mixing events producing mixed layers up to 30 m deep. Between these, the ocean restratified to form very shallow and diurnally varying mixed layers (Zeiden et al. 2024). CALYPSO measurements were made on April 8-10, 2019 in the Mediterranean Sea south of Spain (Mahadevan et al. 2020) during steady winds of 8-13 m/s.

b. Surface Waves

During LCDRI, surface waves were measured by a Datawell Waverider buoy at CDIP station 229 (https://cdip.ucsd.edu/themes/cdip/?d2=p70:s:229) about 70 km west of the operations area and just north of San Nicholas Island and by 8 SWIFT drifters (Thomson et al. 2019) of two different generations at the experimental site. Ma et al. (2020) describes these measurements in detail and compares the different measurements. No significant bias in wave spectra or direction was found between the datasets.

c. Lagrangian Float, ADCP and AHRS

Measurements were made using a Lagrangian float (Fig. 2), a versatile platform for upper ocean observations developed and built at the Applied Physics Laboratory of the University of Washington (D'Asaro 2003; D'Asaro et al. 2014; Shcherbina et al. 2019; Alkire et al. 2012). Here, we used data from Lagrangian float 83 (ADCP serial number 100455) deployed in LCDRI and float 82 (ADCP 100282) in CALYPSO on multiple missions lasting 1-2 days. During LCDRI deployments, the float repeatedly profiled from the surface to 30-50 m at about 0.03 m s^{-1}, typically doing 36 profiles per day of operation. During CALYPSO it followed water parcels within the mixed layer as they repeatedly cycled through the 30-50 m deep mixed layer. Unless otherwise specified, all data shown are from LCDRI.

The float carried a 1 MHz Nortek Signature ADCP (Acoustic Doppler Current Profiler), which included an Inertial Labs OS3DM attitude and heading reference system (AHRS) sampling at 2 Hz. The AHRS measures the acceleration, rotation rate (rate gyros), and magnetic field vectors and

computes the float orientation from these using a proprietary algorithm. The ADCP was mounted at a distance L above the float's center of rotation (Fig. 3) and offset to the side. The center of rotation is not easily measured, so L will be estimated from the AHRS data.

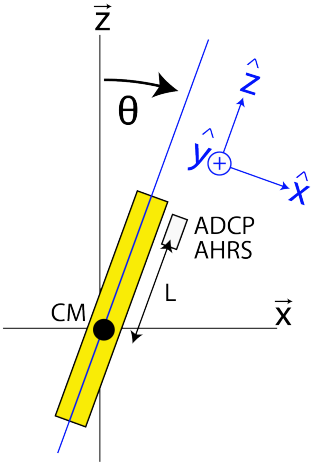

FIG. 3. Lagrangian float frame of reference. A float tilts at an angle θ in the $x-z$ plane defining float coordinates $(\hat{x},\hat{y},\hat{z})$. The tilt is measured by an AHRS unit that is offset along the float by a distance L from the center of rotation.

4. Float and Measurement Kinematics

a. Geometry and Notation

Figure 3 shows the geometry of the float tilt measurements in a vertical $x-z$ plane. The float tilts with angle θ from vertical. Measurements by an AHRS (Attitude and Heading Reference System, see Section 3c) of vector acceleration and rotation rate are made a distance L above the center of rotation. Measured and computed quantities will be represented by capital letters. Thus, the value of θ computed from the horizontal accelerometers is Θ_A. For each measured quantity, $\widehat{X}$ will denote the measured value in the float frame, X the value in the $(\vec{x},\vec{y},\vec{z})$ frame. Physical values, i.e., those described in Section 2, will be represented by lowercase letters; there is only one real tilt, θ.

189 Measurements in the instrument frame are related to those in the earth's frame by

$$\widehat{X_z} = X_z\cos(\theta) + X_x\sin(\theta) \approx X_z + X_x\theta \tag{12}$$

$$\widehat{X_x} = X_x\cos(\theta) - X_z\sin(\theta) \approx X_x - X_z\theta \tag{13}$$

190 *b. Acceleration kinematics*

191 Since the AHRS is mounted above the center of the float (Fig. 3), the measured acceleration is
192 the acceleration of the center of the float plus the acceleration of the AHRS relative to the center
193 due to the angular acceleration of the tilt,

$$\widehat{A_z} = A_z + g, \tag{14}$$

$$\widehat{A_x} = A_x - (A_z+g)\theta + L\frac{d^2\theta}{dt^2} \approx -g\theta + A_x + L\frac{d^2\theta}{dt^2}. \tag{15}$$

194 Note that all accelerometers (including those employed by AHRS) measure gravity as *upward*
195 acceleration $+g$, so it is added to wave-induced acceleration A_z in (14). The term $A_z\theta$ in (15) is
196 quadratic in θ and therefore ignored.

197 At sufficiently low frequencies, the second and third terms in the RHS of (15) are negligible, and
198 the accelerometer accurately measures the tilt as $\Theta = -\widehat{A_x}/g$. More generally, dividing (15) by $-g$
199 defines the "apparent" tilt angle $\Theta_A \equiv -\widehat{A_x}/g$ measured by the accelerometer.

$$\Theta_A = \theta - A_x/g - \omega_L^{-2}\frac{d^2\theta}{dt^2} \tag{16}$$

200 where $\omega_L = \sqrt{g/L}$ is the pendulum frequency. Thus, Θ_A is not the true tilt, but the sum of the true
201 tilt, a term due to lateral acceleration, and a term due to angular acceleration.

202 *c. Rotation Rate Kinematics*

203 The rotation rate around the y axis is

$$\Omega_y = \frac{d\theta}{dt}. \tag{17}$$

Integration of the measured rotation rate in time yields the tilt estimate

$$\Theta_Y(T) = \int_0^T \Omega_y(t)dt + \Theta_0 \tag{18}$$

with integration constant Θ_0. Low frequency measurement noise and gyroscope biases cause Θ_0 to vary on timescales longer than the wave's periods, so Θ_Y is only accurate at high frequencies. In contrast, the noise in Θ_A is most severe at high frequencies, so it is accurate only at low frequencies. Combining these complementray measurements yields measurements at both high and low frequencies. The accuracy of such a "sensor fusion" approach and the frequency limits depend on the noise in the sensors and is analyzed in section 5.

d. Frequency Analysis

The analysis now moves into Fourier space using auto and cross spectra. To transition from the real wave fields discussed in Section 2 to the Fourier space, it is convenient to use their analytic (complex) representation. For example, we express $\zeta \sim \cos(kx - \omega t)$ as the real part of a complex variable $\tilde{\zeta} \sim e^{i(kx-\omega t)}$. After this transformation, the factor of $e^{i(kx-\omega t)+kz}$ becomes common to all expressions (2)-(7), and it will be omitted. Now, (4) and (5) can be written in Fourier space as

$$\underline{a}_z = -\underline{\mathfrak{a}}\omega^2 \tag{19}$$

$$\underline{a}_x = -i\underline{\mathfrak{a}}\omega^2 \tag{20}$$

where $\underline{a}_z$, $\underline{a}_x$ and $\underline{\mathfrak{a}}$ are complex Fourier components and are functions of frequency ω. Fourier components will be underlined to differentiate them from constants or functions of time. In this Fourier-space representation, the time derivatives are replaced by multiplication by $-i\omega$; the derivatives x are replaced by multiplication by ik and the analysis is performed as a function of ω.

We are particularly interested in the spectral characteristics of the various tilt angles (Θ_G, Θ_A, Θ_W, and others). The angle subscripts denote their source: A for acceleration, Y for gyros, I for the AHRS estimate, W for the "wave" estimate, G for effective gravity and Z for vertical acceleration. For any two angles Θ_M and Θ_N, we will compute the corresponding autospectra (S_M, S_N), the crosspectrum C_{MN}, the complex coherence Coh_{MN}; and the transfer function T_{MN} to Θ_M from Θ_N.

The formal definitions are provided in Table 1. Thus, the transfer function from the tilt measured by the accelerometers, $\underline{\Theta}_A$, to that measured by the gyros, $\underline{\Theta}_Y$, is denoted T_{YA}. S and C have units of variance or covariance. They must additionally be normalized by a spectral bandwidth to be cast into the usual spectral units of variance/bandwidth. Coh and T are dimensionless and must be cast into units of 1/bandwidth.

e. Combining Float and Wave Dynamics and Kinematics

Lagrangian floats are neutrally buoyant and thus accurately follow the motion of water parcels larger than the float since as justified in detail by D'Asaro (2003, 2015). We therefore assume that the float's acceleration is the same as the water parcel acceleration, i.e.

$$\underline{A}_z = \underline{a}_z \tag{21}$$

$$\underline{A}_x = \underline{a}_x. \tag{22}$$

Combining (19) - (20) with (21) - (22) yields

$$\underline{A}_x = i\underline{A}_z; \tag{23}$$

horizontal and vertical wave-induced accelerations of the float have the same magnitude, but are 90^o out of phase since the water parcel trajectories are circles. Variations of A_z are accurately measured by the float's accelerometer (see (14)), therefore $\underline{A}_z = \widehat{\underline{A}_z}$. Inserting this into (9), expresses the variations in effective gravity in terms of the measured z acceleration:

$$\underline{\Theta}_G = \underline{a}_x/g = \underline{A}_x/g = i\widehat{\underline{A}_z}/g. \tag{24}$$

Putting (24) back into (16) yields

$$\underline{\Theta}_A = \underline{\theta} - \underline{\Theta}_G + \frac{\omega^2}{\omega_L^2}\theta = \left(1 + \frac{\omega^2}{\omega_L^2}\right)\underline{\theta} - \underline{\Theta}_G, \tag{25}$$

from which we can derive a new 'Wave' estimate of tilt angle θ,

$$\underline{\Theta}_W = (\underline{\Theta}_A + \underline{\Theta}_G)\left(1 + \frac{\omega^2}{\omega_L^2}\right)^{-1}. \tag{26}$$

Importantly, this estimate can be computed from the observed float accelerations ($\widehat{A_x}$, $\widehat{A_z}$) alone, but it is not affected by the wave-induced accelerations like $\underline{\Theta}_A$ (see (16)). This estimate is only possible due to the combined constraints imposed by float dynamics (21, 22) and wave dynamics (23) and will not necessarily apply to other types of platform.

f. Consistency tests

$\underline{\Theta}_W$ and $\underline{\Theta}_Y$ are independent measurements of tilt. We can therefore test the accuracy of our analysis assumptions by comparing their autospectra, transfer functions, and coherences. Multiplying each side of (26) by Θ_Y^* and dividing by $|\underline{\Theta}_Y|^2 = \underline{\Theta}_Y\underline{\Theta}_Y^*$, forms the transfer function

$$T_{WY} = (T_{AY} + T_{GY})\left(1 + \frac{\omega^2}{\omega_L^2}\right)^{-1}. \tag{27}$$

Multiplying (26) by $\underline{\Theta}_W^*$, i.e. finding its squared magnitude, gives the spectrum of $\underline{\Theta}_W$

$$S_W = [\,S_A + S_G + 2\,\Re(C_{AG})\,]\left(1 + \frac{\omega^2}{\omega_L^2}\right)^{-2}, \tag{28}$$

where $\Re$ is the real part. A normalized spectra difference between S_W and S_Y can be formulated as

$$\Delta S_{WY} = 2\frac{S_W - S_Y}{S_W + S_Y}. \tag{29}$$

If $T_{WY} = 1$ and $\Delta S_{WY} = 0$, then the measurements are consistent with the assumptions of the analysis, i.e. two-dimensionality, linear wave dynamics, small angles, and known float geometry. Deviations from this imply that one or more of these assumptions are imperfect.

Similarly, multiplying each side of (26) by $\underline{\Theta}_I^*$ and dividing by $\underline{\Theta}_I\underline{\Theta}_I^*$,

$$T_{WI} = (T_{AI} + T_{GI}) \left(1 + \frac{\omega^2}{\omega_L^2}\right)^{-1}. \tag{30}$$

A normalized spectral difference between S_W and S_I is

$$\Delta S_{WI} = 2\frac{S_W - S_I}{S_W + S_I} \tag{31}$$

If $T_{WI} = 1$ and $\Delta S_{WI} = 0$ then the tilt value computed internally by the AHRS is consistent with the assumptions of the analysis.

5. Analysis and Results

a. Data selection and processing

The analyzes in Sections 2 and 4 assume that the surface waves are two-dimensional, with small tilts, and that the float does not rotate around the z axis and only tilts around the y axis. For real data, this is clearly wrong. We selected and pre-processed the float data to minimize these effects.

First, the acceleration and rotation rate vectors were rotated around the $\hat{z}$ axis to a coordinate frame with the x-axis aligned down-wave using the wave direction computed by the CDIP buoy at a frequency of 0.3 Hz and the float heading measured by the AHRS and corrected for magnetic declination and hard iron effects. Second, only data from the upward profiles were used, since during downward profiles the float typically rotated $30° - 60°$ in a 15 second wave period, enough to invalidate the two-dimensional assumption. Rotation during upward profiles is about $\pm 7.5°$ in 15 seconds as the drogue stays close to the float hull. Finally, the depth range analyzed was chosen to have small yet measurable float tilt angles; a depth range of 10-20 m has typical rms tilts during storms of 0.7° but with 99% of the tilts less than 4° (SM Section 1). Spectral estimates were computed for upward profiling data segments with mean pressures of 10-20 dbar, including only segments with at least 1024 points, and between 5 and 20 m long. FFT's were 512 point long, 50% overlapped with half-cosine (Hann) windows. Auto- and cross-spectra were calculated from the average of all segments in each of the deployments.

b. Data limitations

Our analyzes assume that the float is much smaller than the surface wave scales. In reality, the float size L_f becomes comparable to the inverse wavenumber of the surface wave (wavelength/2π) when $kL_f = 1$, which occurs at about 0.4 Hz for L_f=1.3 m. Therefore, our analyzes will not apply above a frequency of about 0.4 Hz.

Our analyzes assume that the surface wave field is two-dimensional. In reality, waves have a broad downwind directional spectrum that produces cross-wind tilts and thus contaminates the measured value of Ω_y. Indeed, the data shows that Ω_x has magnitudes similar to Ω_y at surface wave frequencies. Furthermore, Ω_z fluctuations are somewhat larger and of lower frequency. This cannot be due to surface waves, which are irrotational and are therefore due to other types of motion. The vertical vorticity of the boundary layer turbulence (Lien et al. 1998) is a likely candidate. Ω_x will also tilt some of Ω_z into Ω_y. These effects will introduce noise into the down-wave component. We will address the importance of this using the consistency tests (Section 5d).

c. Observed Spectra

Figure 4 shows the spectra for 4 deployments selected to have large surface wave signals. The peak surface wave frequency ($\sim$ 0.12 Hz) and the resonant frequency of the float ($\sim$ 0.3 Hz; see Section 6) are marked by dashed vertical lines. The analysis is carried out over a frequency range starting at the lowest wave frequency ($\sim$ 0.05 Hz) and ending where the finite size of the float significantly attenuates the wave signal ($\sim$ 0.45 Hz). Regions outside of this band are shaded.

The autospectra (Fig. 4a) of vertical acceleration Φ_Z (blue thick) rise rapidly to the peak wave frequency and then fall to a white noise floor outside the wave band. In contrast, the autospectra of the tilt from horizontal acceleration Θ_A (red thick) rise to a plateau at the wave peak and remain nearly constant to the resonance frequency, before falling to the same noise floor. The autospectra of tilt from rotation rate Θ_Y (orange thick) rise to the wave peak, decay more slowly to the resonance frequency, and then fall rapidly to levels far below the accelerometer noise floor due to the combined effect of decreasing wave amplitude at high frequencies and the attenuation of the float response due to its finite size (Lien et al. 1998). The coherence magnitude between Θ_A and Θ_Y (Fig. 4b, thick red, AY) is nearly 1 in the wave band, while the phase (Fig. 4d) decreases linearly by about 45^o. The coherence magnitudes of Θ_A or Θ_Y with Φ_Z (AZ-blue and AY-orange) are high at the

frequency of the wave peak, but fall rapidly through the resonance frequency to nearly zero values above the wave band, while their phase increases by about 90° across the wave band. Such large phase changes are expected across the peak for a resonant system. The transfer spectra (Fig. 4c) have a strong peak close to the resonant frequency for all quantities. Overall, the spectra suggest a resonance near 0.3 Hz.

The thin lines in Fig. 4ab show the same spectra for the cross-wave components. The autospectra are somewhat smaller, but the coherences are much smaller, so the phase is noisy and not shown. Perhaps the contributions of waves to the right and left of the down-wave direction cancel. Regardless, the analysis framework does not include these waves, and with little coherence or theory we cannot analyze them further.

d. Consistency Tests: Analysis, sensor and AHRS errors

1) Rotation and Accelerometer Measurements

Fig. 5 evaluates the consistency tests for the down-wave data in Fig. 4 for frequencies within the surface wave band. The coherences AZ, AY and YZ (Fig. 5b) are high throughout the band. In general Θ_W and Θ_Y are close to consistent. The ΔS_{WY} is about 0.08. The imaginary part of T_{WY} is zero within the uncertainty of the four realizations (Fig. 5 d). $\Re(T_{WY})$ is about 3% above 1.0 (Fig. 5c). The remaining inconsistency in ΔS_{WY} and $\Re(T_{WY})$ could be corrected by increasing the magnitude of $\underline{\Theta}_Y$ by 3.5% (Fig.5ac, thin red lines) for unknown reasons.

The value of L is determined from the consistency tests. Varying L adds an upward or downward curvature to $\Re(T_{WY})$ and ΔS_{WY}. For example, using a value of L=0.4 m causes $\Re(T_{WY})$ to bend downward, reaching 1.0 at about 0.33 Hz. We use $L = 0.3$ m with an estimated accuracy of 0.05 m.

Θ_W, Θ_A and Θ_Y were also compared in the laboratory by swinging the AHRS on a variety of pendulums (SM Section 3). The Θ_Y and a Θ_W modified for the laboratory geometry were consistent to a few percent and Θ_Y had a noise level within the surface wave band of a fraction of a degree.

Overall, these results indicate that the combination of careful data selection, rotation in the down-wave direction, and selection of a limited range of frequencies has limited the combined errors from the measurements and in the assumptions of two-dimensionality, linearity and small angles to about 3%. It is surprising that they are this small.

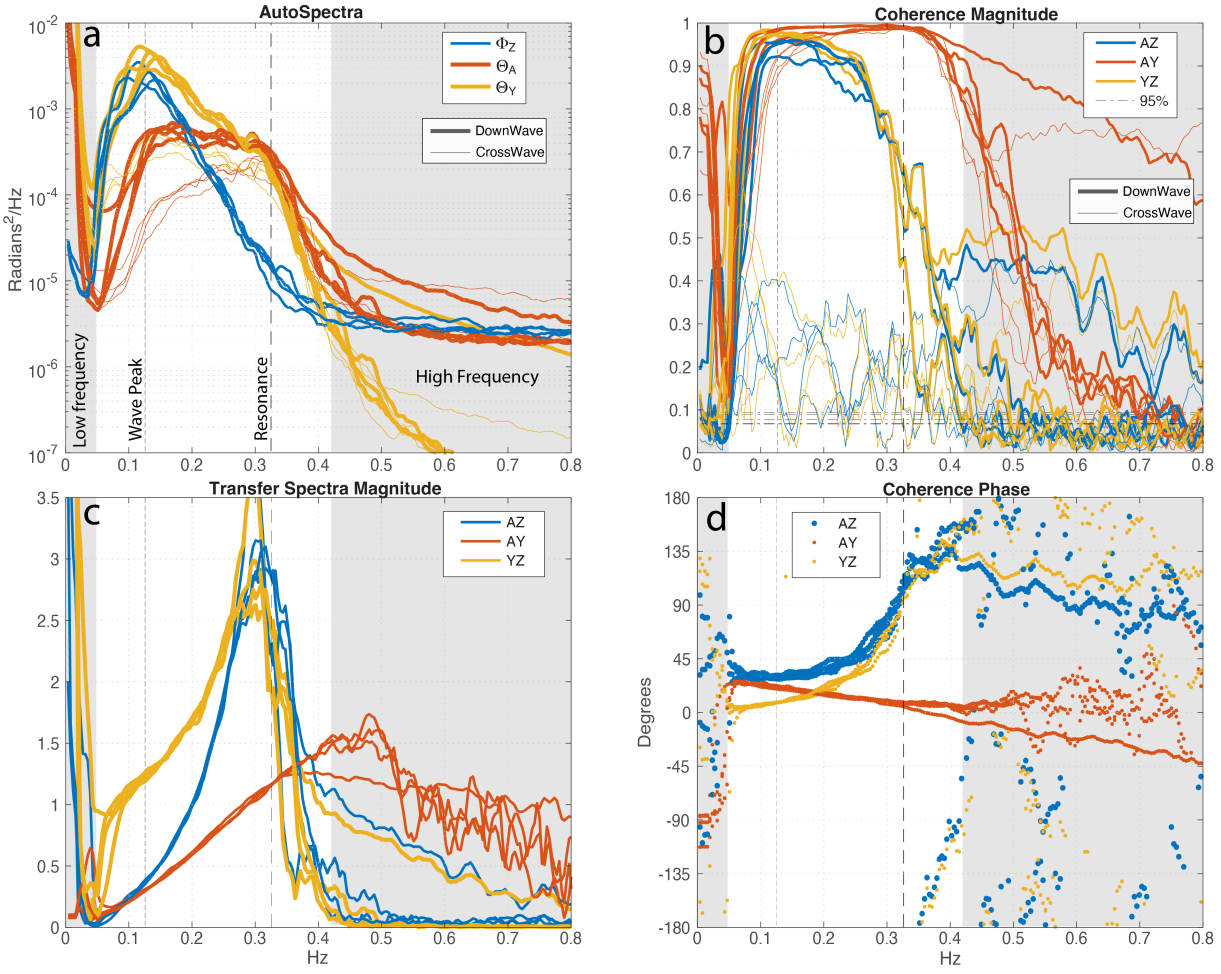

FIG. 4. Tilt spectra from 4 selected float 83 LCDRI deployments with large wave signals. The different realizations provide an estimate of the variability. Data is rotated into down-wave (thick lines) and cross-wave (thin lines) directions. Tilts are computed from different sources: 'A', horizontal acceleration, 'Z' vertical acceleration, and 'Y', integrated rotation rate. Vertical dashed lines indicate float resonance frequency and approximate wave peak. Shading denotes frequencies below the surface wave band, where the wave dynamics analyzed here does not apply, and above about 0.4 Hz, where noise and finite float size begins to dominate the measurements. a) Autospectra for downwave and crosswave tilts. b) Coherence magnitude between different tilt measurements labeled so that 'QR' is transfer from source Q to source R. Horizontal dashed lines shows 95% levels of no significance. c) Transfer function magnitudes. d) Phase for transfer function and coherence.

2) AHRS TILTS

In contrast, Θ_W and Θ_I are not consistent. The real and imaginary parts of T_{WI} and ΔS_{WI} (green lines) are much farther away from the consistent values (black horizontal lines) than could be due

to measurement or sampling uncertainty. We expect Θ_A to accurately measure small tilts at low frequency (16) and use this to test the accuracy of Θ_I under these conditions (SM, Fig. S1b). They agree better than 0.1°. Similarly, we expect Θ_Y to accurately measure the tilts in the surface wave frequency band. This is true to about 0.1° when the tilts are small (SM, Fig. S1c), but not when they are large (SM, Fig. S1d). In laboratory tests, Θ_W and Θ_I are nearly consistent at small tilts. However, at larger tilt angles, the AHRS tilt estimates Θ_I in both field and laboratory data show intermittent, abrupt deviations, which may indicate episodic Kalman filter adjustments in the AHRS algorithm. These results suggest that the AHRS tilts are only reliable for small tilts and suggest some systematic errors even for small tilts. A detailed diagnosis is beyond the scope of this paper.

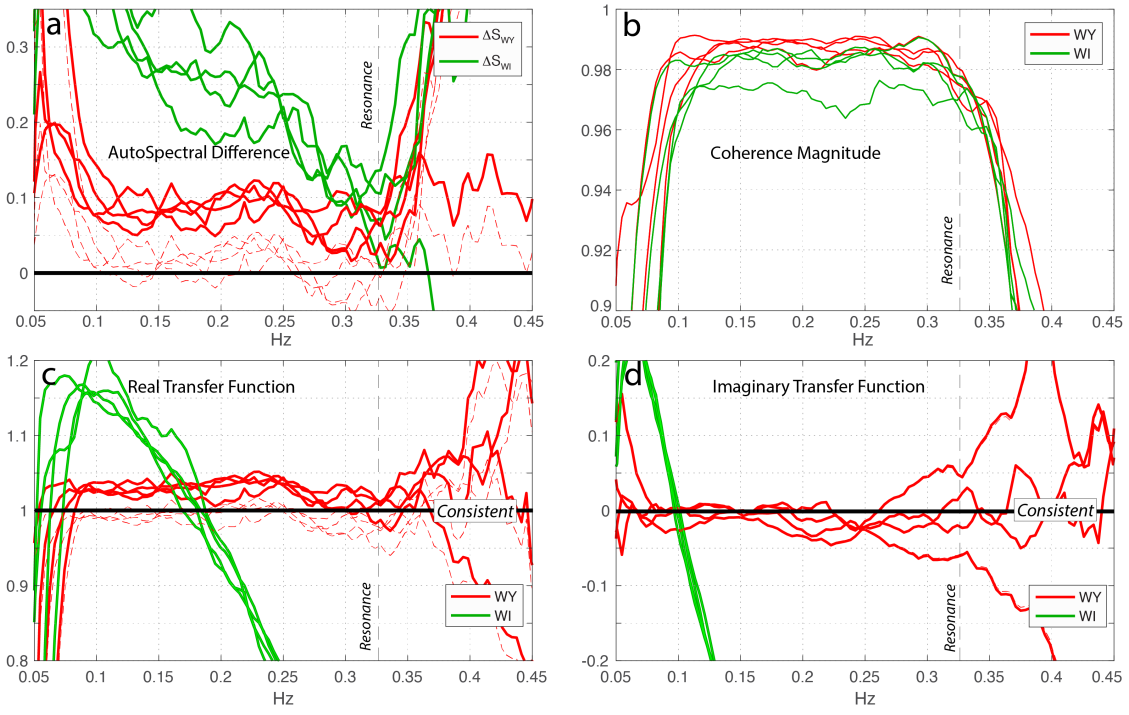

FIG. 5. Consistency tests for spectra in Fig. 4. Each panel shows consistency tests for 4 float deployments: red for WY tests between Θ_W and Θ_Y, and green for WI tests between Θ_W and Θ_I. The results for perfect consistency are indicated by the horizontal black lines. The solid lines show results for the data; the thin dashed lines show results of increasing the gain on the rate gyros by 3.5%. a) Normalized autospectral difference (29) and (31), b) coherence magnitude, Θ_W to Θ_Y (red) and Θ_W to Θ_I (green). c) Real part of transfer function, Θ_W to Θ_Y and Θ_W to Θ_I, equations (27) and (30). d) Same but for imaginary part of transfer function.

6. Float Response Model

a. Dynamics

We wish to predict the wave-induced tilt of a subsurface float within the surface wave frequency band to first order in wave slope. Thus, we do not aim to predict lower frequency tilts such as those caused by low frequency Eulerian shears or the rectified effect of the surface waves, for example Stokes drift, but only the oscillatory response linearly related to the surface waves.

In general, the tilt of a submerged object is governed by a balance of hydrostatic and hydrodynamic torques. The hydrostatic torque arises from the righting moment generated by the float's buoyancy and mass distribution. The hydrodynamic torque results from the interaction between the float's geometry and the strain field of the ambient flow, and can induce rotation even when the surrounding flow is irrotational. A full hydrodynamic simulation of the float is impractical for our goals: we do not need a detailed CFD representation but rather an empirical model that reproduces the observed response function reliably. We do, however, want this model to be physically grounded rather than a simple curve fit. We would like the physical structure constrain the functional form, making the empirical parameters physically meaningful and allowing a degree of interpretability of the results.

A useful point of departure is the idealized theory of Jeffery (1922). Jeffery showed that small, rigid ellipsoids in steady, low-Reynolds-number, irrotational flows undergo rotation governed by the local strain field and tend to align with principal strain directions (see also Junk and Illner 2007), However simple, this theory provides clear mechanistic intuition: wave-induced strain and effective gravity fields act as a time-varying forcing, while buoyancy and weight distribution provide restoring torques. In the case of a time-varying strain field associated with surface gravity waves, the alignment kinematics are generally nonlinear (Ma et al. 2022). In our case of an initially vertical body and under the small-angle approximation, strain-aligned angle can be approximated to first order as

$$\theta_J = -\mathfrak{a} k \lambda e^{kz} \sin(kx - \omega t) = \lambda \theta_Z, \tag{32}$$

where subscript "J" stands for Jeffery's alignment angle (cf. eq.13c of Ma et al. 2022). The shape eccentricity parameter $\lambda \in [-1, 1]$ is defined as $\lambda = (L_\parallel^2 - L_\perp^2)/(L_\parallel^2 + L_\perp^2)$, where $L_\parallel$ and $L_\perp$ are

the diameters parallel and perpendicular to the main axis of symmetry of a body[1]; it describes the range of shapes from a flat disk ($L_\parallel \ll L_\perp$, $\lambda = -1$) to a thin rod ($L_\parallel \gg L_\perp$, $\lambda = 1$).

Equation (32) supports the intuitive notion that, in absence of a righting moment, a thin initially vertical rod would orient itself along the Z-lines ($\lambda = 1 \rightarrow \theta_J = \theta_Z$), while a flat disc would tilt in the opposite direction ($\lambda = -1 \rightarrow \theta_J = -\theta_Z = \theta_G$) and orient itself with the P-lines (so that its axis is aligned with the effective gravity vector $\vec{g}_e$). These two limiting cases of wave-induced tilting correspond to the "inertial" and "hydrostatic" response modes, respectively (Longuet-Higgins 1986). A generically shaped body can be expected to have an intermediate alignment angle described by (32), as discussed by Shcherbina and D'Asaro (2025).

The hydrostatic righting torque always acts to align the float's axis with the effective gravity vector $\vec{g}_e$. Thus, it enhances hydrostatic tilting ($\lambda < 0$) but opposes the inertial response ($\lambda > 0$). A general dynamic model of the float's tilt should therefore include terms accounting for both the hydrodynamic (strain alignment) and hydrostatic (righting moment) torques. Theoretical modeling of these combined effects is challenging due to several factors, including the irregular shape of the float, its finite size, and the potential for turbulent flow. We therefore adopt an empirical approach, guided by observed behavior and the considerations outlined above.

b. Model formulation

We propose an empirical model for the float's tilt in the $x-z$ plane, governed by the balance between the righting torque and the strain-alignment torque:

$$\frac{d^2\theta}{dt^2} = -\sigma^2(\theta - \theta_G) - q\frac{d}{dt}(\theta - \theta_J). \tag{33}$$

The left-hand side represents the change in the angular momentum of the float, i.e. the angular acceleration. The rotational moment of inertia (including any added mass effects) is divided out and absorbed by the right-hand side coefficients. The right-hand side is the sum of the torques discussed in Section 6a, parameterized by empirical linear coefficients. The first term on the right parameterizes the angular acceleration of the float towards the direction of effective gravity θ_G

[1]Even though the original Jeffery (1922) theory was developed for ellipsoid bodies, Bretherton (1962) later demonstrated that it applies to any rotationally-symmetric shape. In such general cases, the parameter λ is interpreted as an effective eccentricity parameter, although its definition is not as straightforward as in the ellipsoidal case.

(9) using the rate parameter σ^2. By itself, this term results in a harmonic oscillation of $\theta - \theta_G$ at frequency σ.

The second term linearly parameterizes the torque due to the misalignment of the float and the wave strain field; it vanishes when the float orientation matches the Jeffery's angle $\theta_J = \lambda\theta_Z = -\lambda\theta_G$. The coefficient q is the ratio between the rotational drag and the rotational moment of inertia of the float. By itself, this term results in an exponential decay of $\theta - \theta_J$ at a rate q. The Jeffery theory underlying this term applies to an infinitesimal particle in a low-Reynolds-number Stokes flow, quite different from that of a finite-sized float in a turbulent boundary layer. An empirical approach to that environment might invoke frictional torques resulting from the asymmetry of the body in the time-dependent wave strain field as $\alpha\frac{d}{dt}(\theta - \theta_Z) + \beta\frac{d}{dt}(\theta - \theta_P)$ where α and β parameterize the drag from the motion of the oppositely tilting Z and P lines. This yields an equation identical to (33), suggesting that this term is a general linear parameterization of the interaction between wave strain and the float asymmetry.

Using (32) and (11), we can rewrite the float tilt model (33) as a linear, damped harmonic oscillator driven by the forcing angle θ_G:

$$\frac{d^2\theta}{dt^2} = -\sigma^2(\theta - \theta_G) - q\frac{d}{dt}(\theta + \lambda\theta_G), \tag{34}$$

or

$$\frac{d^2\theta}{dt^2} + q\frac{d\theta}{dt} + \sigma^2\theta = \sigma^2\theta_G + \kappa\frac{d\theta_G}{dt}, \tag{35}$$

where $\kappa = -\lambda q$. If the float had no righting moment ($\sigma = 0$) and no shape eccentricity ($\lambda = \kappa = 0$), it would not tilt. Rotational drag alone ($q > 0$) does not cause tilt, since the flow field is irrotational; either eccentricity or a righting moment are required. Coefficients σ, q, and κ have dimensions of inverse time and units of $rad\ s^{-1}$, abbreviated as s^{-1}. They are to be determined empirically.

Estimation of the model coefficients is most effectively performed in Fourier space (see section 4d), where (35) becomes

$$-\omega^2\underline{\theta} - i\omega q\underline{\theta} + \sigma^2\underline{\theta} = \sigma^2\underline{\theta}_G - i\omega\kappa\underline{\theta}_G. \tag{36}$$

This corresponds to a transfer function $T_{\theta G}$ from the wave forcing $\underline{\theta}_G$ to the tilt $\underline{\theta}$ of the float

$$T_{\theta G} = \frac{\sigma^2 - i\kappa\omega}{\sigma^2 - \omega^2 - iq\omega} = -\frac{\sigma^2 - i\kappa\omega}{(\omega - \sigma_+)(\omega - \sigma_-)} \tag{37}$$

with the roots of the denominator

$$\sigma_\pm = \sigma(\pm[1 - Q^{-2}]^{0.5} - i/Q) \tag{38}$$

and

$$Q = 2\sigma/q. \tag{39}$$

This is a resonant system with 3 independent parameters: a resonant frequency σ, a quality factor Q describing the sharpness of the resonance, and an asymmetry parameter κ. One might expect this system to be characterized by four parameters specifying the resonance frequency, the damping rate, and the forcing amplitude in terms of θ_G and $d\theta_G/dt$. Our formulation uses only 3, since σ^2 specifies both the resonant frequency and the forcing by θ_G.

c. Model evaluation

The model response $T_{\theta G}$ will be evaluated using Θ_G from (24) and $\underline{\theta}$ from $\underline{\Theta}_Y$ because it has lower noise and a higher signal than $\underline{\Theta}_A$ and does not require the estimation of L. Using (37), the float response model is thus

$$T_{YG} = \frac{\sigma^2 - i\kappa\omega}{\sigma^2 - \omega^2 - iq\omega} \tag{40}$$

Figure 6 shows the fits of the model to the data. The parameters were found by minimizing the summed squared difference between the prediction of the model of T_{YG} and the data, both real and imaginary parts. The fitting was performed over a frequency range of 0.09-0.35 Hz, between the lowest frequency of the surface waves and the frequency at which the gyro- and vertical acceleration measurements become incoherent (Fig. 4). The fittings were performed separately for each float deployment with the variation between deployments used to assess the variability in the parameters. The same 4 cases as in Fig. 4 are shown.

At the resonant peak, the data (black) show a maximum amplitude (Fig. 6a) and a rapid phase change (Fig. 6b). The model (colored lines) fits both features well, but with decreasing accuracy

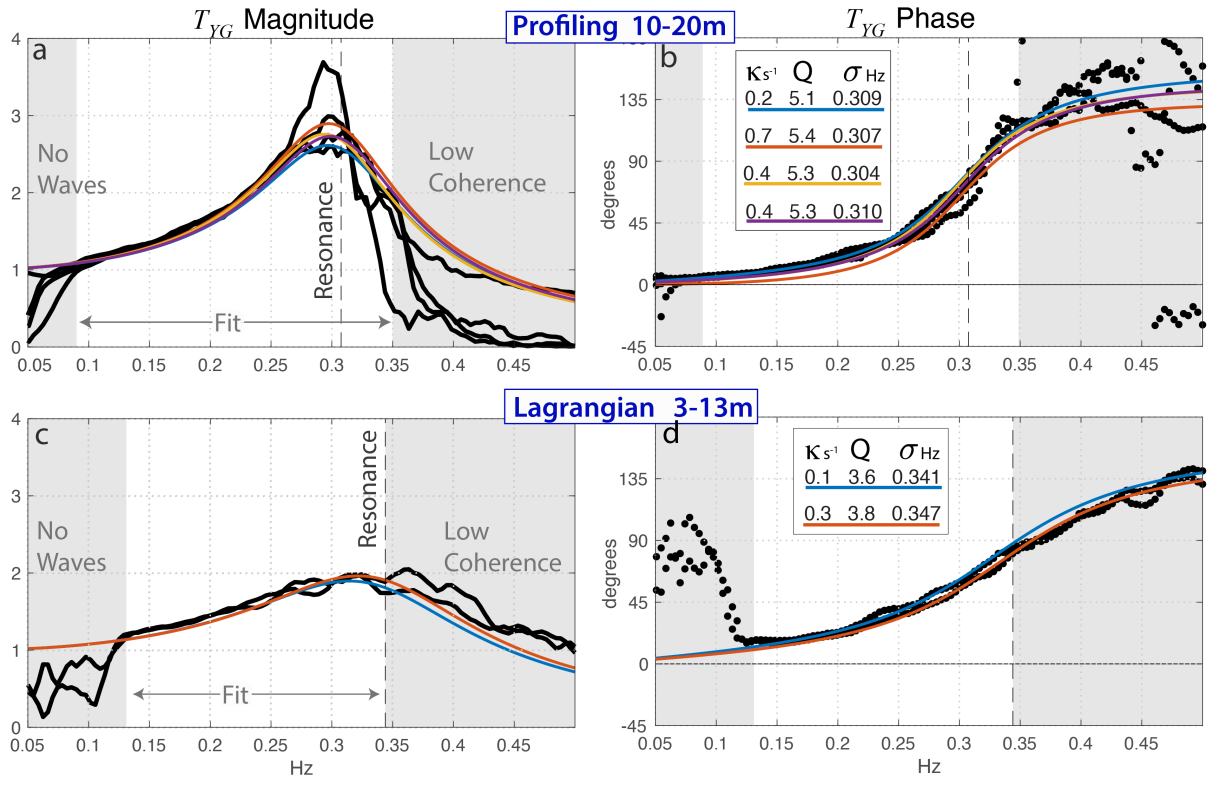

FIG. 6. (a) Magnitude and (b) phase of T_{YG} (40) for data segments in Fig. 4. The same quantities for the CALYPSO data are shown in (c-d). Colored lines are least squares model fit over the white frequency domain. The shaded regions not used for fitting vary between the two deployments due to differences in the peak wave frequency and coherence. Model parameters for each fit are listed in the box.

for frequencies greater than σ due to decreasing coherence. The mean rms deviation of the model from the data is about 10%, 0.2 out of a typical signal of 2. The model indicates that the phase changes from near zero at low frequencies, as the float closely follows the effective gravity, to near 90° at high frequencies, where the angular acceleration balances the drag.

For comparison, the same analysis was performed on about 38 hours of data from a Lagrangian float deployed during the 2019 CALYPSO experiment (Mahadevan et al. 2020) under strong wind forcing (~ 11 m s^{-1}) and relatively short fetch. Unlike the LCDRI float, which profiled with a partially folded drogue and was sometimes in the mixed layer and sometimes beneath it, this float operated in a Lagrangian mode with the drogue open and thus followed the three-dimensional motion of the water, repeatedly crossing the 30-50 m deep mixed layer. Spectra of the CALYPSO float motion (not shown) are similar to those for the LCDRI float, but model fits (Fig. 6cd) yield a

slightly higher resonant frequency, and smaller values of Q. A similar increase in σ and a decrease in Q is found for 2 low-wave data segments from LCDRI.

Table 2 summarizes the parameter fits for the 6 data segments plotted in Fig. 6.

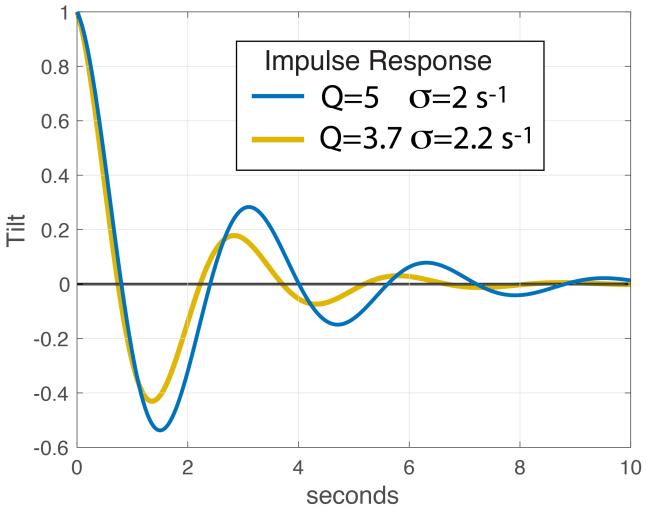

FIG. 7. Impulse response of the float model. Units are normalized to 1 at time=0. Blue: $Q = 5$ and $\sigma = 2 rad\ s^{-1}$, orange: $Q = 3.7$ and $\sigma = 2.2 rad\ s^{-1}$

d. Implications

The values of the derived parameters are reasonable. The resonant frequency $\sigma \approx 2\, s^{-1}$ (3-second period) is equivalent to that of a simple pendulum 0.4 m long, approximately 30% of the float length. The values of $Q = 5$ ($q = 0.6\ s^{-1}$) for LCDRI and $Q = 3.7$ ($q = 1.2\ s^{-1}$) for CALYPSO are consistent with a larger rotational drag in CALYPSO, since the drogue was open. For both, the model implies that the float is somewhat underdamped and will exhibit a decaying oscillation of a few cycles when perturbed (Figure 7). Visual observations of the float when it is on the surface qualitatively show this behavior. For LCDRI, $\kappa = 0.45\ s^{-1}$ and $\lambda = -0.6$, implying a mostly hydrostatic response.The negative sign of the eccentricity parameter λ is surprising, as it corresponds to an equivalent oblate ellipsoid with $L_{\|} : L_{\perp} = 1 : 2$, in stark contrast to the actual prolate geometry of the float's hull ($L_{\|} : L_{\perp} \approx 5 : 1$). The CALYPSO response shows weaker strain alignment and eccentricity parameter closer to zero ($\lambda = -0.2$). This value, by itself, appears to be consistent with a more symmetric shape of the float when its drogue is open. However, the decrease in λ in LCDRI could be due to the closed drogue decreasing $L_{\perp}$ or due to the much larger mean

flow past the float, roughly 0.1 $m\,s^{-1}$ in LCDRI compared to less than $0.01 m\,s^{-1}$, in CAYPSO. Furthermore, the wide range of variability in the best-fit values of λ (ranging from -0.98 to -0.1) suggests that this parameter is poorly constrained by the data or, equivalently, that this parameter has only a small influence on the response function.

7. Summary

Subsurface and nearly neutrally buoyant floats can be stable and well behaved platforms for measuring ocean dynamics in the near-surface wave zone. Here, we investigate and model their motion and tilts. A future paper will model the resulting errors in ADCP measurements following Shcherbina and D'Asaro (2025).

A Nortek Signature1000 ADCP with AHRS (Attitude and Heading Reference System) on a Lagrangian float deployed in the upper ocean in a variety of wind and wave conditions measured the acceleration, magnetic field, and rotation rate of the float. The same AHRS was tested in the laboratory by swinging it on a variety of pendulums with frequencies similar to those of surface waves. We used these data to test the accuracy of various estimates of the float tilt and to generate a model to predict these tilts from surface wave properties as follows:

- Float tilts are assumed to be small, confined to a plane, and driven by linear surface waves. The float is assumed to move with the surface waves.

- Data records are chosen so the tilts are small and the rotation rates around the vertical axis are small enough to be unimportant at surface wave frequencies. Data are rotated, so the analysis plane is aligned downwave. The analyses are conducted in a frequency band between the lowest surface wave frequency and the highest frequency, where the finite float size effects are small.

- The vertical displacements of surface waves are measured from vertical acceleration. Float tilt θ is estimated in three redundant ways: measured rotation rates are integrated to compute Θ_Y. Surface wave dynamics are used to merge vertical and horizontal acceleration and compute Θ_W. The AHRS computes Θ_I using a proprietary algorithm.

- Comparison of these 3 tilt estimates is used to test the accuracy of the measurements, the analysis assumptions and the AHRS algorithm in both the field data and laboratory tests finding:

  - Θ_Y has a noise level low enough to provide accurate measurements of the tilt variations within the surface wave band to a fraction of a degree.
  - Θ_Y and Θ_W are consistent with the assumptions to about 3%, a surprisingly small number.
  - Θ_I is only reliable for small tilts and has clear errors for tilts larger than a few degrees.

- Float tilt is empirically modeled as a linear damped harmonic oscillator driven by linear surface waves. The model has 3 parameters, physically corresponding to the float's righting moment, rotational drag, and shape eccentricity. These yield the resonant frequency, the quality factor Q, and the asymmetry of the coupling to the periodic wave strain field. Since the float follows the nearly circular oscillating trajectories of water parcels beneath surface waves, the effective direction of gravity felt by the float oscillates at the surface wave frequency. Tilts are forced primarily by the float's righting moment continually seeking this direction. The tilt is also forced by the wave strain interacting with the float's shape.

- The model fits the data from multiple float deployments under different conditions to an accuracy of about 10%. The resonant period is about 3 seconds and Q is $3-6$ depending on the float configuration. These Lagrangian floats are thus a somewhat underdamped oscillator and will exhibit a decaying oscillation of a few cycles when perturbed.

8. Discussion

The analysis presented here assumes an idealized float geometry and that the surface waves are two-dimensional and have small slopes. This greatly simplifies the analyses and leads to simple dynamics and remarkably robust results, but limits their generality. Real surface waves have a large directional spread, which can cause float tilts and rotations of similar magnitudes in all directions. Here, a careful choice of data allowed the analysis to minimize these effects and extract and model tilts in the down-wave direction; this is not true under all conditions. However, the results are sufficient to provide a useful tilt response function for understanding the errors in Lagrangian float

measurements, specifically the errors in ADCP measurements resulting from float motion in the wave zone.

A disturbing result of this study is that general purpose AHRS sensors may at times yield very poor estimates of orientation, far worse than their specifications, even if the underlying sensors are providing accurate data. We found that simple tests using pendulums with periods similar to those of surface waves can help detect such problems. Although the AHRS outputs can exhibit large errors and were inconsistent with the constraints imposed by the float geometry and wave forcing, they agreed well with those computed directly from the sensors for small tilts. Apparently, the generic AHRS algorithm used was accurate enough, despite its imperfections. An algorithm that included the constraints of float geometry and wave forcing might yield more accurate results over a wider range of tilts.

The Lagrangian floats characterized here have a resonant frequency within the surface wave band, which amplifies their response to the waves. Since the wave energy decreases rapidly with frequency, float tilting could be significantly decreased if the resonance were moving the resonance out of the wave band. For example, in Fig. 6 the wave forcing at 0.4 Hz is about a factor of 10 less than that at the resonance of 0.31 Hz. Increasing the resonant frequency by this factor of 1.3 would decrease the rms tilt by about a factor of 3. Moving the resonance to below the longest period waves could have a similar effect. Neither can easily be done within other design constraints.

9. Acknowledgements

This work was supported by the Office of Naval Research Departmental Research Initiatives, RIOT, CALYPSO and Langmuir (N00014-24-1-2720,N00014-18-1-2139, N00014-18-1-2420, N00014-14-1-0666, N00014-17-1-2859), and by NASA S-MODE project, an EVS-3 Investigation awarded under NASA Research Announcement NNH17ZDA001N-EVS3. We thank the officers and crew of the R.V. Sproul and R.V. Pourquoi Pas? and the engineering staff of the Applied Physics Laboratory.

10. Data Availability Statement

Field and laboratory data are available at DOI: 10.5061/dryad.70rxwdc96

References

Alkire, M. B., et al., 2012: Estimates of net community production and export using high-resolution, Lagrangian measurements of O_2, NO_3-, and POC through the evolution of a spring diatom bloom in the North Atlantic. *Deep Sea Research Part I: Oceanographic Research Papers*, **64**, 157–174, doi:10.1016/j.dsr.2012.01.012.

Amador, A., S. Jaramillo, and G. Pawlak, 2017: ADCP bias and stokes drift in auv-based velocity measurements. *Journal of Atmospheric and Oceanic Technology*, **34 (9)**, 2029–2042, doi:10.1175/JTECH-D-16-0182.1.

Ardhuin, F., et al., 2019: SKIM, a candidate satellite mission exploring global ocean currents and waves. *Frontiers in Marine Science*, **6**, 209, doi:10.3389/fmars.2019.00209.

Bretherton, F. P., 1962: The motion of rigid particles in a shear flow at low Reynolds number. *Journal of Fluid Mechanics*, **14 (2)**, 284–304, doi:10.1017/S002211206200124X.

Centurioni, L. R., et al., 2019: Global in situ observations of essential climate and ocean variables at the air–sea interface. *Frontiers in Marine Science*, **6**, 419, doi:10.3389/fmars.2019.00419.

D'Asaro, E., 2015: Surface wave measurements from subsurface floats. *Journal of Atmospheric and Oceanic Technology*, **32 (4)**, 816–827, doi:10.1175/JTECH-D-14-00180.1.

D'Asaro, E. and C. McNeil, 2007: Air–sea gas exchange at extreme wind speeds measured by autonomous oceanographic floats. *Journal of Marine Systems*, **66 (1-4)**, 92–109, doi:10.1016/j.jmarsys.2006.06.007.

D'Asaro, E. A., 2003: Performance of autonomous Lagrangian floats. *Journal of Atmospheric and Oceanic Technology*, **20 (6)**, 896–911, doi:10.1175/1520-0426(2003)020<0896:POALF>2.0.CO;2.

D'Asaro, E. A., J. Thomson, A. Shcherbina, R. Harcourt, M. Cronin, M. Hemer, and B. Fox-Kemper, 2014: Quantifying upper ocean turbulence driven by surface waves. *Geophysical Research Letters*, **41 (1)**, 102–107, doi:10.1002/2013GL058193.

D'Asaro, E. A., et al., 2018: Ocean convergence and the dispersion of flotsam. *Proceedings of the National Academy of Sciences*, **115 (6)**, 1162–1167, doi:10.1073/pnas.1718453115.

599 Gould, W. J., 2005: From Swallow floats to Argo - the development of neutrally buoyant floats.
600 *Deep Sea Research Part II: Topical Studies in Oceanography*, **52, 3-4**, 529–543, doi:10.1016/j.
601 dsr2.2004.12.005.

602 Jeffery, G. B., 1922: The motion of ellipsoidal particles immersed in a viscous fluid. *Proc. R. Soc.*
603 *Lond. A*, **102 (715)**, 161–179, doi:10.1098/rspa.1922.0078.

604 Junk, M. and R. Illner, 2007: A new derivation of Jeffery's equation. *J. Math. Fluid Mech.*, **9**,
605 455–488, doi:10.1007/s00021-005-0208-0.

606 Kumar, B. P., E. D'Asaro, M. Ravichandran, et al., 2019: Widespread cooling of the Bay of Bengal
607 by tropical storm Roanu. *Deep Sea Research Part II: Topical Studies in Oceanography*, **168**,
608 104 652, doi:10.1016/j.dsr2.2019.104652.

609 Laxague, N., et al., 2018: Observations of near-surface current shear help describe oceanic oil and
610 plastic transport. *Geophysical Research Letters*, **45 (1)**, 245–249, doi:10.1002/2017GL075891.

611 Lien, R.-C., E. A. D'Asaro, and G. T. Dairiki, 1998: Lagrangian frequency spectra of vertical
612 velocity and vorticity in high-Reynolds-number oceanic turbulence. *Journal of Fluid Mechanics*,
613 **362 (177)**, 104, doi:10.1017/S0022112098008787.

614 Longuet-Higgins, M. S., 1986: Eulerian and Lagrangian aspects of surface waves. *Journal of Fluid*
615 *Mechanics*, **173**, 683–707, doi:10.1017/S0022112086001325.

616 Luyten, J. R. and J. Swallow, 1976: Equatorial undercurrents. *Deep Sea Research and Oceano-*
617 *graphic Abstracts*, Elsevier, Vol. 23:10, 999–1001.

618 Ma, B., E. D'Asaro, S. TB, and T. J, 2020: LC–DRI field experiment and data calibration report.
619 Technical Report APL-UW TR 2002, Applied Physics Laboratory, University of Washington,
620 1013 NE 40th Str, Seattle, WA USA.

621 Ma, K., N. Pujara, and J.-L. Thiffeault, 2022: Reaching for the surface: Spheroidal microswimmers
622 in surface gravity waves. *Phys. Rev. Fluids*, **7**, 014 310, doi:10.1103/PhysRevFluids.7.014310.

623 Mahadevan, A., A. Pascual, D. L. Rudnick, S. Ruiz, J. Tintoré, and E. D'Asaro, 2020: Coherent
624 pathways for vertical transport from the surface ocean to interior. *Bulletin of the American*
625 *Meteorological Society*, **101 (11)**, E1996–E2004, doi:10.1175/BAMS-D-19-0305.1.

626 Menemenlis, D., J. Campin, P. Heimbach, C. Hill, L. T., A. Nguyen, M. Schodlok, and H. Zhang,
627 2008: Ecco2: High resolution global ocean and sea ice data synthesis. *Mercator Ocean Quarterly*
628 *Newsletter*, **October**, 13–21.

629 Phillips, O. M., 1977: *The Dynamics of the Upper Ocean*. 2d ed., Cambridge Univ. Press, Cam-
630 bridge, UK, 344 pp.

631 Pizzo, N., W. Melville, and L. Deike, 2019: Lagrangian transport by nonbreaking and
632 breaking deep-water waves at the ocean surface. *J. Phys.Oceanogr.*, **49 (4)**, 983–992, doi:
633 10.1175/JPO-D-18-0227.1.

634 Pollard, R., 1973: Interpretation of near-surface current meter observations. *Deep Sea Research and*
635 *Oceanographic Abstracts*, Elsevier, Vol. 20,3, 261–268, doi:10.1016/0011-7471(73)90015-6.

636 Sanford, T. B., R. G. Drever, and J. H. Dunlap, 1978: A velocity profiler based on the principles
637 of geomagnetic induction. *Deep sea research*, **25 (2)**, 183–210, doi:10.1016/0146-6291(78)
638 90006-1.

639 Shcherbina, A. Y. and E. A. D'Asaro, 2025: Wave-induced biases in ADCP measurements from
640 quasi-lagrangian platforms. *Journal of Atmospheric and Oceanic Technology*, doi:10.1175/
641 JTECH-D-24-0046.1.

642 Shcherbina, A. Y., E. A. D'Asaro, and R. R. Harcourt, 2019: Rain and sun create slippery layers in
643 the Eastern Pacific fresh pool. *Oceanography*, **32 (2)**, 98–107, doi:10.5670/oceanog.2019.217.

644 Shcherbina, A. Y., E. A. D'Asaro, and S. Nylund, 2018: Observing finescale oceanic velocity
645 structure with an autonomous Nortek acoustic Doppler current profiler. *Journal of Atmospheric*
646 *and Oceanic Technology*, **35 (2)**, 411–427, doi:10.1175/JTECH-D-17-0108.1.

647 Thomson, J., et al., 2019: A new version of the SWIFT platform for waves, currents, and turbulence
648 in the ocean surface layer. *2019 IEEE/OES Twelfth Current, Waves and Turbulence Measurement*
649 *(CWTM)*, IEEE, 1–7, doi:10.1109/CWTM43797.2019.8955299.

650 Torres, H., A. Wineteer, P. Klein, T. Lee, J. Wang, E. Rodriguez, D. Menemenlis, and H. Zhang,
651 2023: Anticipated capabilities of the ODYSEA wind and current mission concept to estimate
652 wind work at the air–sea interface. *Remote Sensing*, **15 (13)**, 3337, doi:10.3390/rs15133337.

653 Wenstrand, D. C., 1979: Measurements of vertical profiles of oceanic current and Richardson
654 number near St. Croix, USVI. *Journal of Hydronautics*, **13 (3)**, 69–76, doi:10.2514/3.48168.

655 Wineteer, A., et al., 2020: Measuring winds and currents with Ka-band doppler scatterometry: An
656 airborne implementation and progress towards a spaceborne mission. *Remote Sensing*, **12 (6)**,
657 1021, doi:10.3390/rs12061021.

658 Zeiden, K., J. Thomson, A. Shcherbina, and E. D'Asaro, 2024: Observations of elevated mixing
659 and periodic structures within diurnal warm layers. *Journal of Geophysical Research: Oceans*,
660 **129 (11)**, e2024JC021 399, doi:10.1029/2024JC021399.

TABLE 1. Symbols used in the Analysis

	General notation
x, y, z	Earth coordinate system
$\hat{x}, \hat{y}, \hat{z}$	Float coordinate system
a	Physical value of some variable a
A	Measured or model value of a in earth frame
$\widehat{A}$	Measured or model value in float frame
$\underline{a}, \underline{a}^*$	Fourier transformed a and complex conjugate
$\Re(\underline{a})$	Real part of $\underline{a}$
	Constants
$g, \vec{g}$	Magnitude of acceleration of gravity, gravity vector
$\mathfrak{a}$	Wave Amplitude (1)
ω, k	Wave frequency, wavenumber
L	Offset of AHRS from float center (Fig. 3)
ω_L	$\sqrt{g/L}$
	Variables
ζ	Surface displacement
ξ, χ	Vertical and horizontal water parcel displacements (6, 7)
w, u	Vertical and horizontal velocities (2, 3)
a, A	Acceleration vector; components $A_x A_y A_z, a_x a_y a_z$
Ω	Rotation rate vector; components $\Omega_x, \Omega_y, \Omega_z$
ΔS_{WY}	Consistency test (29)
	Angles
θ	True tilt of float axis relative to vertical (z)
θ_G	Tilt of the effective gravity vector (9)
θ_Z	Tilt of Z-lines (11) = -θ_G
θ_P	Tilt of P-lines (10) = $\frac{\pi}{2} + \theta_G$
θ_J	Jeffery alignment angle (32)
Θ_A	Float Tilt from Horizontal Acceleration (16)
Θ_Y	Float Tilt from Gyros (18)
Θ_I	Float Tilt computed by AHRS
Θ_W	Tilt from acceleration and wave dynamics (26)
	Spectral quantities
"M" and "N" below specify arbitrary angle subscripts (A, Y, I, W)	
S_M	AutoSpectrum of Θ_M; =($\underline{\Theta}_M\ \underline{\Theta}_N^*$)=($\lvert\underline{\Theta}_M\rvert^2$)
C_{MN}	CrossSpectrum of Θ_M and Θ_N; =($\underline{\Theta}_M\ \underline{\Theta}_N^*$)
Coh_{MN}	Complex coherence; =$C_{MN}/(S_M S_N)^{\frac{1}{2}}$
T_{MN}	Transfer function to Θ_M from Θ_N; =(C_{MN}/S_N)
	Float Model Parameters
σ	Restoring rate toward Θ_G; Approximate resonance freq.
q	Rotational drag rate
λ	Eccentricity
κ	= -λ q
Q	= 2σ/q, Resonance Quality factor

Float Model Parameters			
	Mean ± Variation		
$\frac{\sigma}{2\pi}$	0.32	± 7%	Hz
σ	2.01	± 7%	$rad\ s^{-1}$
Q	4.75	±19%	
q	0.88	±27%	s^{-1}
κ	0.37	±82%	s^{-1}
λ	−0.47	±95%	

TABLE 2. Mean values of the model parameters for the 6 model fits in Fig 6. Variation is given as half of the maximum - minimum parameter value as a percentage of the mean.